Contrib Mineral Petrol (1999) 135: 355–372 © Springer-Verlag 1999

Huai-Jen Yang · Frederick A. Frey
David A. Clague · Michael O. Garcia

Mineral chemistry of submarine lavas from Hilo Ridge, Hawaii: implications for magmatic processes within Hawaiian rift zones

Received: 8 July 1998 / Accepted: 2 January 1999

Abstract The crustal history of volcanic rocks can be inferred from the mineralogy and compositions of their phenocrysts which record episodes of magma mixing as well as the pressures and temperatures when magmas cooled. Submarine lavas erupted on the Hilo Ridge, a rift zone directly east of Mauna Kea volcano, contain olivine, plagioclase, augite ±orthopyroxene phenocrysts. The compositions of these phenocryst phases provide constraints on the magmatic processes beneath Hawaiian rift zones. In these samples, olivine phenocrysts are normally zoned with homogeneous cores ranging from ~ Fo_{81} to Fo_{91}. In contrast, plagioclase, augite and orthopyroxene phenocrysts display more than one episode of reverse zoning. Within each sample, plagioclase, augite and orthopyroxene phenocrysts have similar zoning profiles. However, there are significant differences between samples. In three samples these phases exhibit large compositional contrasts, e.g., Mg# $[100 \times Mg/(Mg+Fe^{+2})]$ of augite varies from 71 in cores to 82 in rims. Some submarine lavas from the Puna Ridge (Kilauea volcano) contain phenocrysts with similar reverse zonation.

The compositional variations of these phenocrysts can be explained by mixing of a multiphase (plagioclase, augite and orthopyroxene) saturated, evolved magma with more mafic magma saturated only with olivine. The differences in the compositional ranges of plagioclase, augite and orthopyroxene crystals between samples indicate that these samples were derived from isolated magma chambers which had undergone distinct fractionation and mixing histories. The samples containing plagioclase and pyroxene with small compositional variations reflect magmas that were buffered near the olivine + melt ⟹Low-Ca pyroxene + augite + plagioclase reaction point by frequent intrusions of mafic olivine-bearing magmas. Samples containing plagioclase and pyroxene phenocrysts with large compositional ranges reflect magmas that evolved beyond this reaction point when there was no replenishment with olivine-saturated magma. Two of these samples contain augite cores with Mg# of ~71, corresponding to Mg# of 36–40 in equilibrium melts, and augite in another sample has Mg# of 63–65 which is in equilibrium with a very evolved melt with a Mg# of ~30. Such highly evolved magmas also exist beneath the Puna Ridge of Kilauea volcano. They are rarely erupted during the shield building stage, but may commonly form in ephemeral magma pockets in the rift zones.

The compositions of clinopyroxene phenocryst rims and associated glass rinds indicate that most of the samples were last equilibrated at 2–3 kbar and 1130–1160 °C. However, in one sample, augite and glass rind compositions reflect crystallization at higher pressures (4–5 kbar). This sample provides evidence for magma mixing at relatively high pressures and perhaps transport of magma from the summit conduits to the rift zone along the oceanic crust-mantle boundary.

H.-J. Yang (✉)[1]
Department of Geology, Florida International University, Miami, FL 33199, USA

F.A. Frey
Department of Earth, Atmospheric and Planetary Sciences, Massachusetts Institute of Technology, Cambridge, MA 02139, USA

D.A. Clague
Monterey Bay Aquarium Research Institute, PO BOX 628, 7700 Sandholdt Road, Moss Landing, CA 95039-0628, USA

M.O. Garcia
Department of Geology and Geophysics, University of Hawaii, Honolulu, HI 96822, USA

Present address:
[1] SciLab Boston Inc., Weymouth, MA 02189, USA

Supplementary Material Full set of compositional data for the minerals has been deposited in electronic form and can be obtained from http://link.springer.de/link/service/journals/00410

Editorial responsibility: T.L. Grove

Introduction

Typically during ascent from the mantle to the crust a basaltic magma cools, partially crystallizes, mixes with other basaltic magma and interacts with wallrocks. This complex history is recorded by the mineralogy and compositions of phenocrysts. For example, studies of phenocrysts were essential in establishing the importance of magma mixing in the petrogenesis of ocean floor basalts (e.g., Dungan and Rhodes 1978; Rhodes et al. 1979; Kuo and Kirkpatrick 1982), but phenocrysts in ocean island basalts have not been as intensively studied. Our goal is to use phenocryst compositions in Hawaiian lavas to understand the processes occurring in Hawaiian rift zones. During the main shield building stage, a shallow magma chamber fed by a central conduit is maintained at depths of ~ 2 to 7 km (e.g., Ryan et al. 1981; Klein et al. 1987). The shields grow as magmas are erupted at the summit or injected into the prominent rift zones that radiate from the summit (e.g., Tilling and Dvorak 1993). Magmas erupt along these rift zones from localized vents at varying distances, often tens of kilometers, from the summit. Within this magma plumbing system there are abundant opportunities for magma mixing (Fig. 1). For example, Rhodes (1988) inferred that the compositional homogeneity of Mauna Loa summit lavas indicates eruption from a long-lived, steady-state summit magma reservoir with magma composition buffered at the reaction point of olivine + melt $\Longrightarrow$low-Ca pyroxene + augite + plagioclase. This buffering reflects a balance between differentiation and frequent magma replenishment of the summit reservoir. Magma mixing is also an important rift zone process. Because shield-stage magmatism involves varying magma supply rates (Dvorak and Dzurisin 1993), pockets of magma may become isolated at various depths within the rift zones when magma supply rate decreases. Evolved magma compositions with relatively low MgO contents form as these pockets cool and differentiate. Some of these evolved magmas may proceed beyond the reaction point at which olivine dissolves to form low-Ca pyroxene. When magma supply rate increases, new magma migrates from the summit reservoir or conduit into rift zones where it can mix with residual evolved magmas (Clague et al. 1995; Garcia et al. 1992; Helz and Wright 1992; Murata and Richter 1966; Wright and Fiske 1971).

Most of the well documented cases for mixing of Hawaiian lavas are for lavas erupted at the active volcanoes, Kilauea and Mauna Loa. Preliminary study of phenocryst compositions in olivine-rich tholeiitic basalts dredged (> 1.6 km water depth) from the Hilo Ridge, a submarine rift zone east of Mauna Kea volcano, found examples of reversely zoned plagioclase and pyroxene phenocrysts; i.e., the phenocryst cores equilibrated with a more evolved melt composition (lower Mg/Fe and Ca/Na) than the phenocryst rims (Yang et al. 1994). Although these tholeiitic basalts were assumed to be derived from Mauna Kea volcano, some of their geochemical characteristics extend the range previously observed for Mauna Kea lavas, e.g., to lower $^{143}Nd/^{144}Nd$ and La/Yb (Lassiter et al. 1996; Yang et al. 1994). Such differences may reflect temporal changes

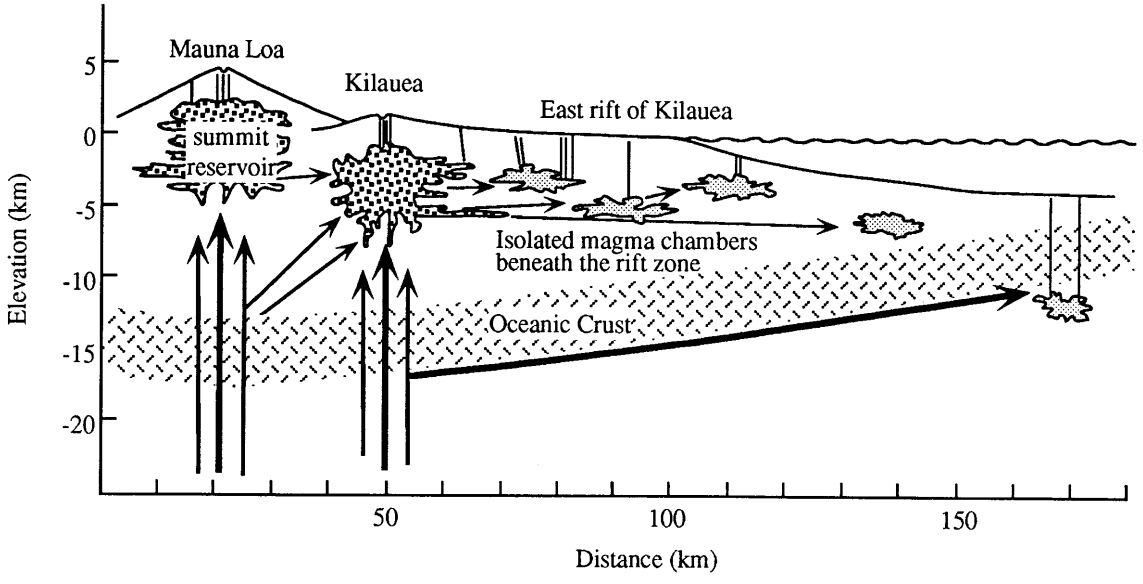

Fig. 1 Inferred pathways (*arrows*) for magma ascent beneath Kilauea and Mauna Loa volcanoes. At each volcano, a central conduit feeds a summit reservoir at 2 to 7 km below the surface. The summit reservoir can be a single chamber or a group of interconnected pockets (Tilling and Dvorak 1993). Magmas migrate laterally from the summit reservoir into the rift zones and when magma supply rate decreases isolated magma chambers can form in rift zones at depths of 2–7 km. Lateral magma movement from the central conduit into rift zones may also occur at deeper levels, such as the oceanic crust-mantle boundary (Garcia et al. 1995). As discussed in the text there are many possibilities for magma mixing within this magma plumbing system

during growth of the Mauna Kea shield or alternatively that shallow lavas forming the Hilo Ridge are from Mauna Kea volcano whereas the deeper lavas, >1100 m, are from Kohala volcano (Reiners et al. 1997). The source of Hilo Ridge lavas is not the focus of this paper; rather we use compositional zoning of phenocrysts in these lavas to understand magma evolution in Hawaiian rift zones. In particular, we establish an important role for magma mixing where one component is a highly evolved magma that is not commonly erupted during shield building. We also estimate the temperatures (1130–1190 °C) and pressures (typically 1–3 kbar with one sample at 4–5 kbar) of phenocryst formation. The sample equilibrated at the highest pressure erupted most distant from the summits of Mauna Kea and Kohala (Fig. 2), and it may have bypassed the summit magma reservoir. In addition, its bulk-rock composition reflects formation by a relatively lower extent of melting and melt segregation at a relatively high pressure (Yang et al. 1994). Finally, comparisons of phenocryst compositions in lavas from the Hilo Ridge, the Puna Ridge of Kilauea volcano and the Southwest Rift of Mauna Loa volcano show that similar mixing processes involving a low MgO melt component occurred in the Hilo and Puna Ridges.

Fig. 2 Dredge locations of the studied submarine lavas from the rift zone east of Mauna Kea volcano. Bathymetric contour interval is 1 km. *Triangles* indicate volcano summits. The subaerial surface of Mauna Kea volcano is covered by the postshield Hamakua Volcanics and younger Laupahoehoe Volcanics. *Inset* shows the location of other prominent rift zones, the Puna Ridge of Kilauea volcano and the Southwest rift of Mauna Loa volcano

Samples

Samples were dredged from 1.6 to 3.3 km water depth on the Hilo Ridge (Fig. 2). Samples designated MK were described by Garcia et al. (1989) and those designated SU were described by Moore (1966), Moore and Fiske (1969), and Moore and Clague (1992). These submarine samples are pillow lavas with quenched glass rinds which represent melt compositions. Based on their whole-rock compositions, Yang et al. (1994) defined two groups. These groups form different trends in MgO variation diagrams with group 1 lavas having lower abundances of incompatible elements than group 2 lavas at a given MgO content. These geochemical characteristics were interpreted as olivine accumulation trends for distinct melt compositions. This paper presents new data for olivine compositions from six samples. Five samples, including two group 1 samples, SU-21-64 and MK2-1, two group 2 samples, SU-20-64 and MK1-8, and a sample with an unusually low SiO_2 content, SU-22-64, were selected for a detailed study of plagioclase and pyroxene phenocryst compositions.

Analytical techniques

Olivine, plagioclase, augite and orthopyroxene were analyzed with the 4-spectrometer JEOL 733 Superprobe at Massachusetts Insti-

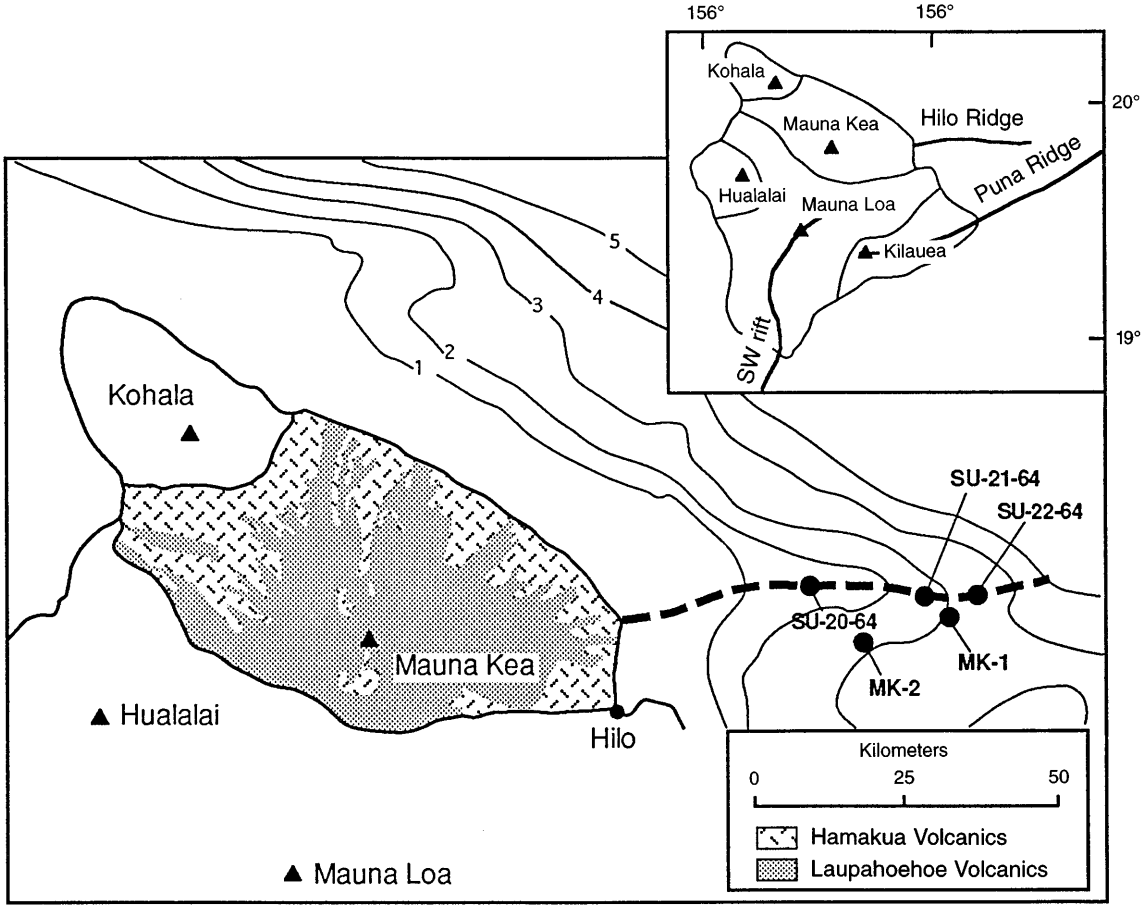

tute of Technology, using 15 keV accelerating voltage, 10 nA beam current and a beam size of 1 μm. Data were reduced using Bence and Albee (1968) matrix corrections with the modifications of Albee and Ray (1970). Compositions were determined on core to rim traverses across orthopyroxene, augite and plagioclase. The typical distance between two analysis points was usually ≤20 μm. Because olivine is not complexly zoned, only the cores and rims were analyzed. Analytical precision for the major oxides was reported in Juster and Grove (1989). The reproducibilities were within ±0.2 for the Mg# [molar Mg × 100/(Mg + Fe)] of pyroxenes and ±0.3 for the anorthite content (An%) of plagioclase. All analyses are consistent with mineral stoichiometry. For example, pyroxene analyses have cation numbers within a range of 4.00 ± 0.02, mostly within 4.00 ± 0.01, on a 6 oxygen basis. The Fo% of analyzed olivines are shown in Fig. 3 and representative analyses of augite, plagioclase, and orthopyroxene are listed in Tables 1 to 3. The complete compositional data set for the minerals is available as an electronic supplement.

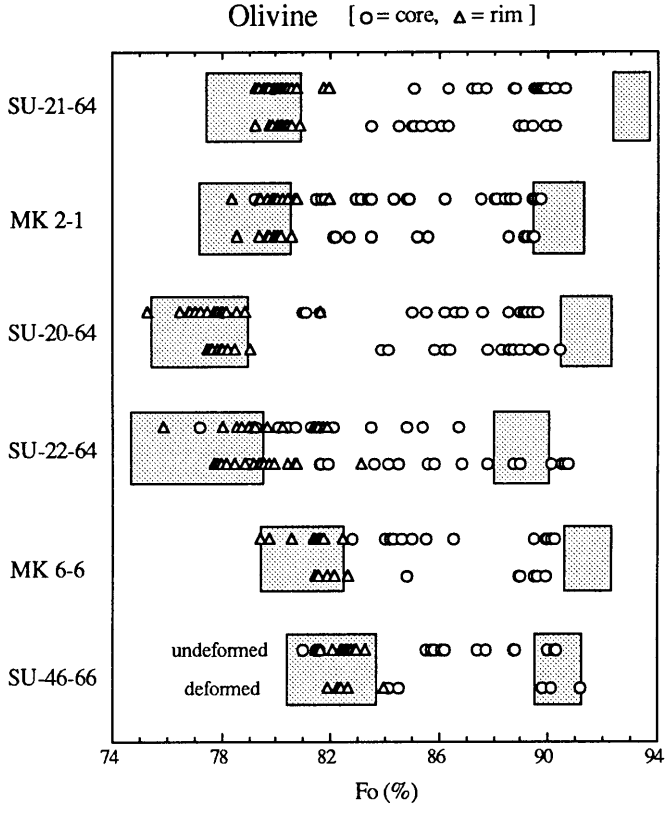

Fig. 3 Olivine compositions for six dredged Hilo Ridge submarine samples. *Circles* are core compositions and *triangles* are rim compositions. For each sample, the *lower line* of data points is for deformed grains and *upper line* is for undeformed grains. The *boxes* at the high Fo end are olivine compositions in equilibrium with whole-rock compositions; those at the low Fo end are in equilibrium with glass compositions (Fe-Mg exchange K_D = 0.3 ± 0.03 and ferrous iron = 85% of total iron for glass). Although the rim compositions are generally in equilibrium with the glasses, the cores are highly variable in Fo and range to values that would be in equilibrium with a melt having the whole-rock compositions. However, the whole-rock compositions represent mixtures (Yang et al. 1994) rather than melt compositions. Many of these Fo-rich olivines may be disaggregate dunites (Clague et al. 1995)

Petrography and mineral compositions

The five samples studied in detail contain olivine, spinel, plagioclase, augite and orthopyroxene. The proportions of phenocrysts (>0.7 mm) and microphenocrysts (0.7–0.1 mm) in these samples are listed in the Table 1 of Yang et al. (1994). Olivine is the most abundant phenocryst and microphenocryst (18–33 vol.%). Plagioclase and augite usually occur as microphenocrysts with plagioclase (3–9 vol.%) slightly more abundant than augite (2–6 vol.%). Orthopyroxene is rare, 1–5 grains in each thin section (8 cm^2), except for SU-22-64 which has ~3% orthopyroxene, i.e., ~15 grains in a thin section. Spinel (<1 vol.%) appears as inclusions in olivine, and was not analyzed.

Olivine

In these samples, 15 to 38% of the olivine grains exhibit deformation textures such as planar extinction discontinuities and rectangular subgrain boundaries (Table 4). Although most of the deformed olivines are subhedral to anhedral and the undeformed grains are usually euhedral to subhedral, both deformed and undeformed olivine crystals occur as a variety of crystal forms ranging from euhedral to resorbed and skeletal (Table 4). Multigrain olivine aggregates are common, as are spinel and melt inclusions in olivine. Except for one weakly reversely zoned grain ($Fo_{80.0–80.5}$) in SU-46-66, all analyzed olivines are normally zoned. Frey et al. (1991) reported two reversely zoned olivines in MK1-3 ($Fo_{78.5–82.2}$ and $Fo_{80.1–82.9}$) and one in MK5-13 ($Fo_{82.6–84.2}$). In all samples, olivine compositions have two common characteristics: (1) core Fo compositions span a wide range, from Fo_{77} to Fo_{91}; (2) rim compositions vary over relatively narrow ranges, mostly Fo_{75} to Fo_{84} and are, in general, in equilibrium with the compositions of the glassy pillow rims (Fig. 3). There is no correlation between core composition, crystal form or size.

Augite

Augite appears as euhedral to rounded phenocrysts and microphenocrysts. They occur as single crystals or form aggregates with plagioclase (Fig. 4A). Augite-olivine clots are only found in SU-22-64, where they are associated with orthopyroxene (Fig. 4H). Except for MK2-1 and MK1-8, augite also forms rims enclosing orthopyroxene (Fig. 4C, F and G). In contrast to augite in Kilauea lavas (Clague et al. 1995; Helz and Wright 1992) and Mauna Loa submarine lavas (Garcia et al. 1995) sector-zoned augite was not found in these submarine lavas.

In general, Na_2O, TiO_2, Al_2O_3 and MnO abundances increase with decreasing Mg# while Cr_2O_3 content and Mg# are positively correlated. Unlike the normal zoning

Table 1 Representative microprobe analyses of augite (Cpx) from Hilo Ridge submarine lavas

		SiO_2	TiO_2	Al_2O_3	Cr_2O_3	FeO	MnO	MgO	CaO	Na_2O	Total	Mg#
SU-21-64												
Cpx-1	Core	51.49	1.00	2.06	0.01	10.57	0.27	15.33	18.50	0.27	99.49	72.1
	Rim	53.08	0.65	1.99	0.56	6.35	0.12	17.92	19.32	0.22	100.22	83.4
Cpx-2	Core	51.42	1.08	2.28	0.02	10.61	0.27	15.35	18.62	0.34	99.99	72.1
	Rim	51.93	0.75	2.80	0.79	7.20	0.18	18.34	17.92	0.23	100.15	81.9
Cpx-3	Core	51.83	1.06	2.20	0.02	10.62	0.28	15.33	18.90	0.36	100.59	72.0
	Rim	51.39	0.95	3.67	0.94	7.24	0.16	17.50	17.72	0.25	99.82	81.2
Cpx-5	Core	51.50	0.95	2.29	0.15	8.78	0.21	16.61	18.90	0.27	99.65	77.1
	Rim	52.17	0.68	2.88	0.97	6.16	0.16	17.46	19.75	0.24	100.47	83.5
Cpx-6	Core	51.80	1.07	2.40	0.18	9.99	0.30	15.81	18.76	0.28	100.60	73.8
	Core	51.97	0.90	2.41	0.23	8.31	0.20	16.73	18.90	0.24	99.88	78.2
	Rim	51.91	0.77	3.11	0.92	6.53	0.17	17.49	18.84	0.30	100.04	82.7
Cpx-7	Core	51.97	1.07	2.75	0.14	9.29	0.19	17.11	17.51	0.24	100.26	76.7
	Core	51.84	0.98	2.52	0.13	9.61	0.24	16.14	18.48	0.30	100.25	75.0
	Rim	51.93	0.87	3.08	0.87	7.00	0.19	17.26	18.82	0.25	100.27	81.5
Cpx-9	Core	51.74	0.97	2.17	0.00	10.97	0.32	15.20	18.73	0.27	100.37	71.2
	Rim	53.08	0.67	1.93	0.66	6.30	0.19	18.07	19.28	0.18	100.37	83.6
Cpx-10[a]	Rim	52.79	0.66	2.00	0.69	6.36	0.17	18.06	18.79	0.26	99.79	83.5
	Rim	51.10	1.13	3.55	0.45	8.68	0.22	18.17	16.32	0.23	99.85	78.9
Cpx-11[a]	Rim	51.68	1.01	3.53	0.63	8.66	0.22	18.91	15.49	0.24	100.35	79.6
MK2-1												
Cpx-1	Core	51.66	0.97	3.50	1.05	7.41	0.22	17.99	16.97	0.20	99.97	81.2
	Rim	53.24	0.64	1.81	0.64	6.65	0.17	18.51	17.91	0.20	99.76	83.2
Cpx-2	Core	50.84	1.41	3.90	0.59	8.68	0.25	17.47	16.47	0.23	99.84	78.2
	Rim	52.87	0.76	2.24	0.49	7.79	0.21	17.89	17.55	0.21	100.00	80.4
Cpx-3	Core	50.50	1.41	3.58	0.33	9.17	0.22	17.57	16.46	0.20	99.45	77.4
	Rim	51.70	0.80	2.67	0.65	7.01	0.17	17.54	18.35	0.23	99.13	81.7
Cpx-5	Core	50.37	1.56	4.19	0.63	7.36	0.20	16.31	18.89	0.22	99.72	79.8
	Rim	51.73	0.85	3.07	1.06	6.45	0.19	17.26	18.52	0.20	99.32	82.7
Cpx-6	Core	52.05	0.91	2.86	0.78	6.64	0.18	16.77	19.54	0.20	99.93	81.8
Cpx-7	Core	52.13	0.75	2.80	0.61	6.65	0.19	17.45	18.90	0.23	99.69	82.4
SU-20-64												
Cpx-1	Core	51.52	1.06	2.43	0.15	9.65	0.22	15.88	18.79	0.27	99.96	74.6
	Rim	51.25	1.02	3.22	0.72	7.46	0.21	16.80	19.03	0.29	99.99	80.1
Cpx-2	Core	52.49	0.86	2.25	0.48	8.81	0.28	18.33	16.49	0.26	100.24	78.8
Cpx-3[a]	Rim	51.63	1.00	3.29	0.73	8.39	0.23	17.57	17.27	0.32	100.43	78.9
Cpx-5	Core	51.15	1.30	2.88	0.05	11.00	0.29	15.37	18.13	0.32	100.49	71.4
	Rim	51.62	1.09	3.36	0.73	7.64	0.22	16.91	18.89	0.30	100.75	79.8
Cpx-6[a]	Rim	51.28	1.20	3.41	0.21	7.81	0.18	16.87	18.75	0.26	99.97	79.4
Cpx-15[b]	Core	51.88	1.05	2.24		9.13		16.22	19.00	0.36	99.88	76.0
	Core	52.19	0.87	1.98		8.62		16.52	18.91	0.31	99.39	77.4
	Rim	52.84	0.63	1.89		7.09		17.79	18.75	0.30	99.28	81.7
Cpx-16[b]	Core	51.55	1.11	2.77		8.40		16.67	18.97	0.28	99.74	78.0
	Rim	53.27	0.64	1.58		8.66		19.62	15.41	0.29	99.46	80.2
Cxp-17[b]	Core	51.20	0.71	1.50		14.20		14.08	17.23	0.32	99.24	63.9
	Rim	51.50	1.02	2.85		7.95		17.53	17.82	0.26	98.94	79.7
MK1-8												
Cpx-1	Core	51.86	0.90	2.34	0.75	6.99	0.20	17.36	18.43	0.27	99.11	81.6
Cpx-3	Core	51.01	1.30	3.71	0.95	6.56	0.19	16.16	19.95	0.27	100.09	81.5
Cpx-5	Core	52.10	0.91	2.57	0.81	7.37	0.16	17.71	17.91	0.26	99.79	81.1
Cpx-131[b]	Core	51.01	1.05	2.59		9.05		17.41	17.26	0.17	98.53	77.4
	Core	50.33	1.43	3.13		10.02		15.43	18.55	0.35	99.23	73.3
	Rim	51.51	0.99	2.70		7.19		16.94	19.14	0.31	98.77	80.8
Cpx-129[b]	Core	52.89	0.74	1.84		8.52		18.59	16.34	0.24	99.16	79.6
	Rim	52.85	0.71	1.69		6.49		17.65	19.12	0.17	98.67	82.9
Cpx-132[b]	Core	50.21	1.54	2.98		11.47		15.16	18.29	0.41	100.06	70.2
	Rim	51.88	1.06	2.41		7.97		16.78	18.57	0.20	98.88	79.0
Cpx-133[b]	Core	50.70	1.48	2.95		9.89		15.46	18.40	0.41	99.28	73.6
	Rim	52.02	0.97	2.31		8.16		17.02	17.83	0.27	98.58	78.8
Cpx-136[b]	Core	51.83	1.15	2.13		10.09		15.72	18.66	0.21	99.78	73.5
	Rim	52.26	0.98	2.42		7.34		17.55	17.92	0.33	98.80	81.0
SU-22-64												
Cpx-2	Core	52.36	0.92	2.69	0.97	5.91	0.15	17.44	19.58	0.33	100.35	84.0
Cpx-1	Core	52.29	0.78	2.76	1.03	5.55	0.07	17.28	20.16	0.29	100.21	84.7
Cpx-3	Core	50.28	1.30	3.97	0.98	5.86	0.13	15.17	21.83	0.31	99.83	82.2
Cpx-5	Core	51.55	1.10	3.19	0.55	7.05	0.11	15.98	20.54	0.32	100.39	80.2
Cpx-6	Core	51.77	1.15	2.60	0.71	7.60	0.11	16.54	19.49	0.34	100.30	79.5
Cpx-7	Core	51.97	0.70	2.76	1.08	5.23	0.10	17.02	20.25	0.23	99.34	85.3

[a] Indicates augite rims enclosing orthopyroxene
[b] Indicates analyses where Cr_2O_3 and MnO were not measured, which result in low totals

Table 2 Representative microprobe analyses of plagioclase (Pl) from Hilo Ridge submarine lavas

		SiO_2	Al_2O_3	FeO	MgO	CaO	Na_2O	K_2O	Total	An (%)
SU-21-64										
Pl-1	Core	55.10	27.97	0.79	0.13	11.32	4.67	0.14	100.12	56.8
	Rim	52.44	29.77	0.87	0.29	13.49	3.48	0.09	100.43	67.8
Pl-2	Core	54.01	28.88	0.81	0.18	12.04	4.35	0.12	100.39	60.1
	Rim	51.75	30.56	0.75	0.19	13.87	3.21	0.07	100.40	70.2
Pl-3	Core	53.83	29.40	0.68	0.12	11.96	4.38	0.13	100.49	59.7
	Rim	54.11	28.80	0.81	0.26	12.16	3.94	0.09	100.18	62.7
Pl-101	Core	51.91	30.29	0.63	0.07	13.39	3.47	0.17	99.93	67.4
	Core	50.30	31.33	0.59	0.07	14.37	2.86	0.12	99.62	73.0
Pl-98	Core	55.12	28.23	0.63	0.04	11.19	4.65	0.28	100.15	56.2
	Rim	53.82	29.06	0.68	0.05	11.97	4.33	0.21	100.12	59.7
Pl-99	Core	53.47	29.16	0.62	0.05	12.10	4.22	0.29	99.91	60.3
	Rim	52.94	29.55	0.65	0.05	12.91	3.88	0.23	100.21	63.9
Pl-104	Core	54.59	28.28	0.61	0.05	11.18	4.65	0.33	99.69	56.0
	Rim	51.96	30.52	0.60	0.07	13.82	3.28	0.15	100.40	69.4
Pl-110	Core	54.04	28.93	0.61	0.05	11.90	4.31	0.31	100.15	59.3
	Rim	50.62	30.88	0.62	0.08	14.04	2.94	0.18	99.35	71.8
Pl-s-1	Core	52.49	29.51	0.79	0.09	13.01	3.67	0.18	99.71	65.5
	Rim	51.26	30.50	0.69	0.08	13.90	3.10	0.16	99.69	70.6
Pl-s-2	Core	51.18	30.84	0.71	0.07	13.89	3.18	0.21	100.09	69.8
	Rim	50.92	29.88	0.77	0.08	13.51	3.96	0.19	99.31	64.7
Pl-s-3	Core	53.18	28.45	0.92	0.16	12.76	3.86	0.23	99.56	63.8
	Rim	51.17	30.72	0.66	0.08	14.09	3.03	0.17	99.91	71.3
MK2-1										
Pl-1	Core	52.68	29.47	0.83	0.32	13.18	3.58	0.12	100.19	66.6
	Rim	51.63	29.84	0.75	0.31	13.58	3.16	0.09	99.36	70.0
Pl-2	Core	51.67	30.69	0.71	0.25	13.87	3.21	0.09	100.49	70.1
	Rim	51.77	30.23	0.80	0.27	13.75	3.33	0.10	100.25	69.2
Pl-3	Core	51.41	30.74	0.54	0.24	13.78	3.27	0.09	100.06	69.6
	Rim	52.57	29.73	0.89	0.26	13.25	3.62	0.10	100.42	66.6
Pl-s-1	Core	52.11	30.18	0.85	0.14	13.63	3.23	0.07	100.21	69.7
	Rim	52.75	29.53	0.89	0.13	13.15	3.55	0.26	100.25	66.2
Pl-s-2	Core	52.54	29.52	0.87	0.14	13.19	3.49	0.27	100.01	66.6
	Rim	51.93	30.51	0.75	0.11	13.69	3.05	0.27	100.30	70.2
SU-20-64										
Pl-0	Core	53.46	29.16	0.80	0.05	12.21	4.23	0.44	100.35	59.9
	Rim	52.11	30.20	0.82	0.08	13.30	3.65	0.24	100.40	65.9
Pl-126	Core	54.46	28.29	0.75	0.04	11.36	4.48	0.53	99.91	56.6
	Rim	53.03	29.57	0.69	0.09	12.71	3.72	0.29	100.11	64.3
Pl-19	Core	52.71	30.06	0.65	0.08	13.25	3.51	0.22	100.48	66.7
	Rim	52.70	30.12	0.63	0.09	13.41	3.45	0.18	100.58	67.5
Pl-109	Core	52.00	29.63	0.77	0.11	12.51	3.90	0.37	99.29	62.5
	Rim	51.76	30.50	0.71	0.08	13.80	3.19	0.16	100.21	69.9
Pl-180	Core	56.49	27.41	0.65	0.02	10.20	5.06	0.47	100.28	51.3
	Rim	52.79	29.11	0.77	0.08	13.10	3.53	0.38	99.76	65.7
Pl-s-1	Core	53.59	28.95	0.71	0.10	12.21	3.96	0.32	99.83	61.8
	Rim	51.84	30.00	0.79	0.10	13.65	3.50	0.27	100.15	67.2
Pl-s-2	Core	53.46	29.15	0.79	0.09	12.21	3.97	0.26	99.91	62.0
	Rim	52.51	29.92	0.84	0.08	13.10	3.58	0.33	100.35	65.6
Pl-1	Core	53.38	29.25	0.74	0.09	12.30	4.18	0.12	100.05	61.5
Pl-2	Core	53.34	29.30	0.77	0.22	12.39	4.07	0.13	100.22	62.2
	Rim	52.82	29.77	0.84	0.21	12.58	3.80	0.16	100.18	64.1
Pl-3	Core	55.22	27.53	1.12	0.30	11.18	4.71	0.14	100.21	56.3
	Rim	56.62	27.91	1.11	0.32	11.16	3.00	0.13	100.25	66.7
SU-22-64										
Pl-2	Core	50.79	31.30	0.60	0.17	14.29	3.09	0.10	100.35	71.5
	Rim	52.68	29.91	0.70	0.22	12.89	3.72	0.16	100.28	65.1
Pl-3	Core	52.54	29.65	0.77	0.22	12.97	3.65	0.10	99.90	65.9
	Rim	50.60	31.25	0.79	0.17	14.67	2.84	0.07	100.39	73.8
Pl-4	Core	52.23	30.47	0.64	0.19	13.12	3.56	0.14	100.35	66.5
	Rim	52.05	30.52	0.68	0.19	13.23	3.65	0.15	100.47	66.1
Pl-1-1	Core	52.14	30.05	0.46	0.08	13.52	3.73	0.19	100.17	66.0
	Rim	49.24	31.64	0.54	0.07	15.14	2.62	0.12	99.36	75.7
Pl-5	Core	51.59	30.71	0.58	0.06	13.29	3.28	0.26	99.77	68.1
	Rim	53.07	28.98	0.80	0.07	12.40	4.17	0.37	99.85	60.9
Pl-6	Core	51.01	30.64	0.58	0.06	13.80	3.28	0.27	99.64	68.8
	Rim	52.85	29.60	0.64	0.06	12.93	3.88	0.32	100.27	63.6

Table 2 (Contd.)

		SiO_2	Al_2O_3	FeO	MgO	CaO	Na_2O	K_2O	Total	An (%)
Pl-7	Core	51.81	30.08	0.63	0.06	13.41	3.53	0.34	99.86	66.4
	Rim	53.03	29.26	0.70	0.06	12.34	4.06	0.37	99.83	61.3
Pl-8	Core	51.92	30.27	0.53	0.06	13.36	3.40	0.29	99.83	67.3
	Rim	50.43	31.06	0.54	0.06	14.22	2.99	0.22	99.51	71.6
Pl-9	Core	52.16	30.17	0.61	0.07	13.07	3.72	0.27	100.07	65.0
	Rim	52.81	29.01	0.84	0.08	12.70	3.93	0.34	99.70	62.9
Pl-10	Core	51.99	29.89	0.57	0.06	12.97	3.62	0.28	99.38	65.4
	Rim	52.56	29.99	0.61	0.06	12.49	3.70	0.33	99.74	63.8
	Rim	51.17	30.61	0.62	0.07	13.80	3.24	0.25	99.76	69.2

of olivine crystals, all analyzed augite crystals show at least one episode of reverse zoning. The compositional variations in an augite crystal can be divided into two types. Type I crystals show abrupt changes from nearly homogeneous Fe-rich cores to Mg-rich rims (Fig. 5, panels A, B, C) resulting in a strong contrast in back-scattered electron images (Fig. 4A). Based on an Fe-Mg exchange K_D of 0.25 $\pm$ 0.2 (Grove and Juster 1989), the Mg-rich rims (Mg# ~78–84) are in equilibrium with the glass rinds, whereas the cores are too enriched in Fe (e.g., SU-21-64 and SU-20-24 in Fig. 6). Type II crystals are relatively homogeneous with core to rim Mg# fluctuating by ~5 units or less (Fig. 5D). Their compositions are similar to the rims of type I crystals (Fig. 6).

For SU-21-64 and SU-20-64, most augite crystals belong to type I. In sample SU-21-64, thirteen of the fourteen analyzed augite grains have homogeneous cores varying within 2 Mg# unit, and in sample SU-20-64 augite cores vary in Mg# from 63 to 80 (Fig. 6). The Mg-rich rims (Mg# 76–84) on all augites in these two samples are in equilibrium with the glass (Fig. 6). In contrast, augite crystals in samples MK2-1 and SU-22-64, are of type II, and the entire grain is, in general, in equilibrium with the glass rinds (Fig. 6). Both compo-

Table 3 Representative microprobe analyses of orthopyroxene (Opx) from Hilo Ridge submarine lavas

		SiO_2	TiO_2	Al_2O_3	Cr_2O_3	FeO	MnO	MgO	CaO	Na_2O	Total	Mg#
SU-21-64												
Opx-1	Core	54.45	0.55	1.33	0.02	15.55	0.32	26.16	2.04	0.03	100.45	75.0
	Core	54.09	0.55	1.30	0.05	16.17	0.30	25.80	2.07	0.03	100.36	74.0
	Rim	55.68	0.33	1.22	0.27	11.19	0.21	29.24	2.36	0.02	100.52	82.3
Opx-2	Core	53.79	0.57	1.39	0.12	16.34	0.35	25.46	1.94	0.06	100.01	73.5
	Rim	55.01	0.45	1.94	0.47	11.11	0.23	28.69	2.50	0.02	100.41	82.1
Opx-3	Core	54.63	0.45	1.17	0.07	14.76	0.29	26.95	2.19	0.03	100.52	76.5
	Rim	55.34	0.34	1.05	0.21	11.36	0.19	29.10	2.36	0.03	99.98	82.0
MK2-1												
Opx-1	Core	54.68	0.55	1.51	0.26	12.00	0.24	28.43	2.21	0.07	99.94	80.9
		55.19	0.50	1.38	0.25	11.65	0.22	28.62	2.09	0.03	99.91	81.4
SU-20-64												
Opx-1	Core	53.25	0.59	1.43	0.07	18.01	0.41	24.59	2.02	0.07	100.43	70.9
MK1-8												
Opx-110	Core	53.69	0.44	0.84	0.09	15.34	0.27	26.47	2.15	0.08	99.37	75.5
	Rim	53.73	0.52	0.99	0.24	15.02	0.30	26.67	2.18	0.08	99.71	76.0
Opx-36	Core	54.02	0.48	1.07	0.16	14.43	0.31	26.97	2.08	0.06	99.58	76.9
	Rim	53.60	0.58	1.41	0.18	14.62	0.27	26.46	2.14	0.03	99.27	76.3
Opx-126	Core	54.04	0.45	1.74	0.50	12.15	0.20	28.15	2.42	0.05	99.70	80.5
	Rim	53.01	0.68	1.48	0.19	15.03	0.26	26.36	2.59	0.03	99.63	75.8
SU-22-64												
Opx-1	Core	54.54	0.58	1.36	0.11	13.21	0.25	27.45	2.26	0.04	99.79	78.7
	Core	54.54	0.57	1.44	0.20	12.93	0.34	27.77	2.27	0.08	100.15	79.3
Opx-2	Core	55.37	0.38	0.96	0.15	12.59	0.29	28.33	2.21	0.04	100.31	80.1
Opx-3	Core	54.91	0.44	1.61	0.35	11.74	0.25	28.70	2.17	0.05	100.23	81.3
Opx-5	Core	53.53	0.67	1.43	0.04	16.69	0.33	25.18	2.29	0.03	100.19	72.9
Opx-6	Core	55.12	0.43	1.36	0.39	11.19	0.23	29.04	2.15	0.06	99.98	82.2
Opx-7	Core	54.86	0.44	1.24	0.25	11.93	0.23	28.74	2.29	0.06	100.03	81.1
Opx-8	Core	54.37	0.55	1.45	0.32	14.34	0.30	26.74	2.00	0.02	100.09	76.9
Opx-9	Core	55.05	0.40	1.48	0.39	10.97	0.21	28.98	2.28	0.09	99.85	82.5
Opx-10	Core	55.20	0.54	1.37	0.41	10.96	0.21	29.44	2.15	0.06	100.35	82.7
Opx-11	Core	55.06	0.41	1.40	0.28	11.20	0.25	28.75	2.30	0.04	99.70	82.1

Table 4 Percentage of deformed and undeformed olivine from Hilo Ridge submarine lavas

Sample	Undeformed			Deformed			Total counted
	Euhedral	Subhedral	Anhedral	Euhedral	Subhedral	Anhedral	
SU-21-64	38.6	17.0	11.3	5.7	15.9	11.4	88
MK2-1	60.3	14.2	10.6	3.5	3.5	7.8	141
SU-20-64	35.2	35.2	5.5	5.5	10.9	7.8	128
MK1-8	31.2	24.7	7.5	4.3	11.8	20.4	93
SU-22-64	23.7	27.8	10.3	8.3	19.6	10.3	97
MK5-13	57.5	15.0	3.9	9.8	11.1	2.6	153
MK6-6	60.4	12.5	6.3	10.4	8.3	2.1	96
SU-46-66	17.0	54.7	11.3	0.0	9.4	7.5	53

sitional types of augite crystals occur in sample MK1-8 (Fig. 6).

Plagioclase

Plagioclase phenocrysts are locally resorbed, sometimes deeply embayed (Fig. 4B) and microphenocrysts are usually euhedral. Like augite, the analyzed plagioclases show reverse zoning with two types of compositional variations; type I crystals exhibit clear compositional difference between cores and rims and type II crystals do not (Fig. 7). Both types occur in samples SU-21-64 and SU-20-64. In these two samples, type I crystals have rims generally in equilibrium with the glass rinds while their cores are relatively enriched in Ab component, ranging from An_{51} to An_{64} (Fig. 8). The type II crystals are usually euhedral and in these two samples each crystal has An content varying within 6%, except for one grain in SU-21-64. Their compositions are similar to that of the An-rich rims on type I grains (Fig. 8). All of the analyzed plagioclase grains in sample MK2-1 belong to type II with compositions varying from An_{66} to An_{71}. Although the plagioclase crystals in sample SU-22-64 show greater compositional variations than the type II crystals in other samples, we classify them as type II owing to the absence of core-rim contrast in their back-scattered images. Their compositions vary from An_{60} to An_{76} (Fig. 8).

Orthopyroxene

Most of the orthopyroxene crystals are anhedral except for some grains in samples MK1-8 and SU-22-64 which are subhedral to euhedral. In samples MK1-8 and MK2-1 orthopyroxene occurs as single crystals with plagioclase inclusions in the latter (Fig. 4D). In sample SU-20-64, four orthopyroxene grains are enclosed by an augite rim with some plagioclase laths in the augite rim. Three orthopyroxene grains are found in the thin section of SU-21-64. Back-scattered images show that parts of the orthopyroxene core are rimmed by Mg-rich orthopyroxene and some parts are rimmed by augite (Fig. 4C). More complex orthopyroxene-augite associations occur in sample SU-22-64. Some euhedral and subhedral orthopyroxene phenocrysts are rimmed by fine-grained augite crystals (Fig. 4E), while other subhedral and anhedral orthopyroxenes are enclosed by an embayed augite rim (Fig. 4F). Occasionally, anhedral orthopyroxene crystals are surrounded by fine-grained augite crystals and then mantled by euhedral augite (Fig. 4G). An unusual orthopyroxene-augite cluster has an anhedral augite microphenocryst mantled by anhedral orthopyroxene which is surrounded by fine-grained augite that is enclosed by fine-grained olivines (Fig. 4H).

In each sample, the compositional zonation of orthopyroxene crystals is similar to that of their coexisting augite. For example, compare Figs. 5A and 9A for sample SU-21-64 and Figs. 5D and 9B for sample MK2-1. In sample SU-21-64 the cores are either homogeneous or slightly normally zoned with Mg# <77 while the Mg-rich rims (Mg# >79) are in equilibrium with the composition of glass rinds (Fig. 10). In sample SU-20-64, the orthopyroxene grains are relatively enriched in Fe (Mg# $\sim$70, Fig. 10). These crystals are enclosed by augite (Fig. 4C) whose composition is in equilibrium with the glass rinds (Fig. 6). Except for two Fe-rich grains (Mg# <78), the Mg# of analyzed orthopyroxene grains in SU-22-64 ranges from 78 to 83 with only a small variation within each grain. Sample MK1-8 contains three orthopyroxene crystals which show at least one episode of reverse zoning with Mg# varying from 74 to 81 (Fig. 10).

►

Fig. 4A–H Back-scattered electron images: **A** An augite-plagioclase clot (×40) in sample SU-21-64. Plagioclase is resorbed and augites show compositional contrast between cores and rims. **B** A locally resorbed plagioclase with deep embayments from sample SU-20-64 (×40). **C** In sample SU-21-64 a rounded orthopyroxene enclosed by more magnesian orthopyroxene and augite rims (×200). **D** A rounded orthopyroxene in MK2-1 with plagioclase and glass inclusions (×60). **E–H** from sample SU-22-64: **E** anhedral orthopyroxene enclosed by fine-grained augites and olivines (×40); **F** Anhedral orthopyroxene with an embayed augite rim (×60); **G** a rounded orthopyroxene enclosed by fine-grain augites, and mantled by euhedral augite (×120); **H** an anhedral augite rimmed by orthopyroxene, and enclosed by fine-grained augites and olivines (×170); the outermost layer contains fine-grained olivines

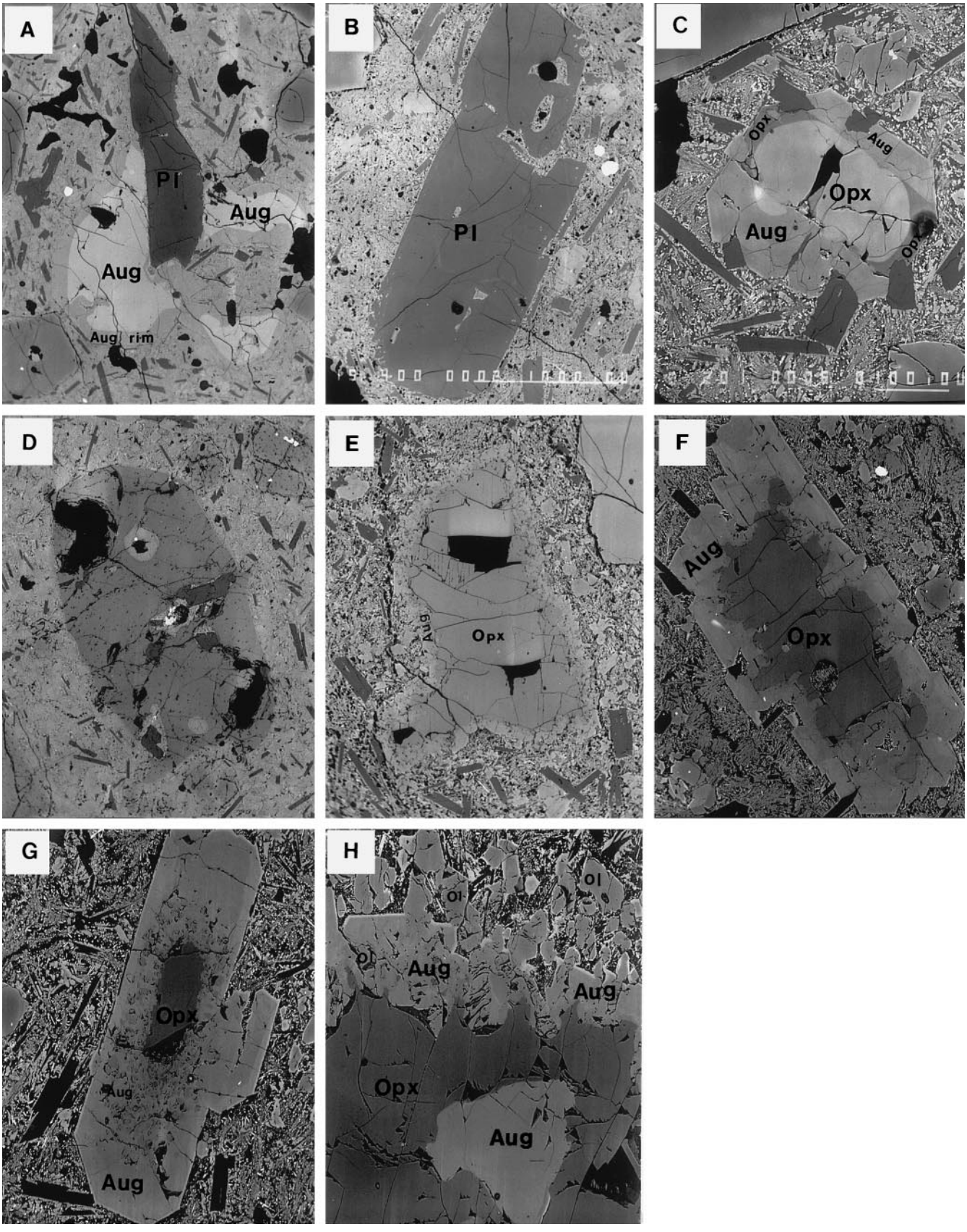
A
Pl
Aug
Aug
Aug rim
B
Pl
C
Opx
Aug
Opx
Aug
Opx
D
E
Aug
Opx
F
Aug
Opx
G
Opx
Aug
Aug
H
Ol
Ol
Ol
Aug
Aug
Opx
Aug

Discussion

Magma mixing in isolated magma chambers

The reversely zoned augite, orthopyroxene and plagioclase phenocrysts in these submarine lavas provide strong evidence for magma mixing (Figs. 5–10). The occurrence of orthopyroxene crystals rimmed by augite is also consistent with magma mixing. Experimental studies of Kilauea lavas show that low-Ca pyroxene is a late crystallizing phase forming after augite and plagioclase at low pressures (e.g., Helz and Thornber 1987). Because the glass rinds on these submarine Hilo Ridge lavas have compositions similar to Kilauea glasses (Garcia et al. 1989; Garcia 1996), it is inferred that low-Ca pyroxene is also a late crystallizing phase in these submarine lavas. Therefore, augite rims enclosing orthopyroxene grains reflect a change from more evolved (orthopyroxene-saturated) to less evolved (orthopyroxene-undersaturated) melt compositions; a result that is consistent with replenishment of a partially crystallized magma chamber by a mafic magma.

The phenocrysts with the most complex compositional zonation provide the most information on magma evolution. The studied Hilo Ridge samples require more than one episode of magma recharge (Figs. 5, 7 and 9), but each sample reflects a distinctly different magmatic history. Samples SU-20-64 and SU-21-64 contain plagioclase and pyroxene phenocrysts with large and abrupt steps of reverse zonation; phenocrysts in sample MK2-1 show only modest changes in core to rim composition and sample SU-22-64 has nearly homogeneous pyroxenes but the plagioclase phenocrysts show two abrupt steps of reverse zonation (Figs. 5–10). The distinctive magmatic histories recorded in the phenocrysts are consistent with the presence of isolated magma chambers along this rift zone. We conclude that lavas erupted along the Hilo Ridge were derived from several different magma chambers which contained evolved magmas that were mixed with more mafic magmas. This inference is similar to conclusions made for the east rift of Kilauea volcano (Clague et al. 1995; Garcia et al.

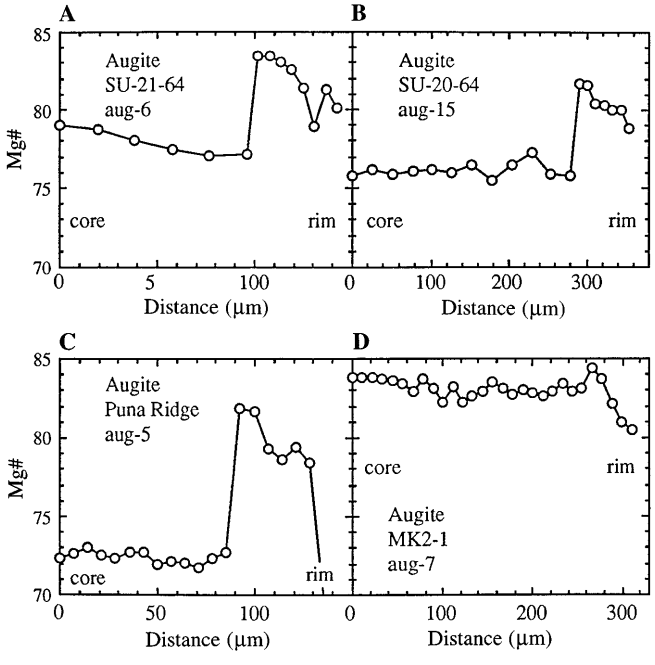

Fig. 5A–D Representative compositional zonation patterns of augite: **A, B** and **C** show large compositional contrasts between cores and rims which are referred to as type I in text; **D** shows the type II variation which is relatively homogeneous with Mg# fluctuating within a small range

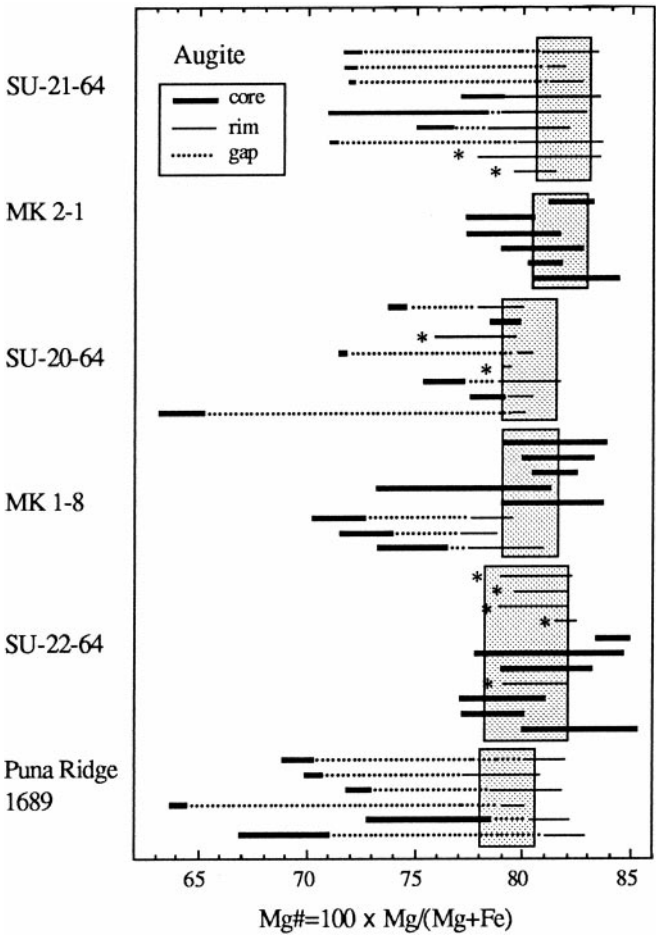

Fig. 6 Augite compositions for five submarine lavas dredged from Hilo Ridge and one sample from Kilauea's Puna Ridge. A *horizontal line* indicates the compositional variation in a grain. When the core and rim show compositional contrast in back scattered images (Fig. 4), the compositional range for core is indicated by a *thick solid line* and that for rim is indicated by a *thin solid line*. A *dotted line* indicates the compositional gap between core and rim. In some samples there is little compositional contrast between rims and cores; for these samples the compositional ranges are indicated by *thick solid lines*. The *boxes* are compositions in equilibrium with the associated glass rinds calculated for an Fe-Mg exchange $K_D = 0.25 \pm 0.2$ (Tormey et al. 1987; Grove et al. 1992). For a melt composition, ferrous iron is assumed to be 85% of total iron. The range of the equilibrium composition for SU-22-64 is based on the two glass compositions reported by Yang et al. (1994), while those for other samples are calculated for one glass composition. The * symbol indicates augite rims enclosing orthopyroxene

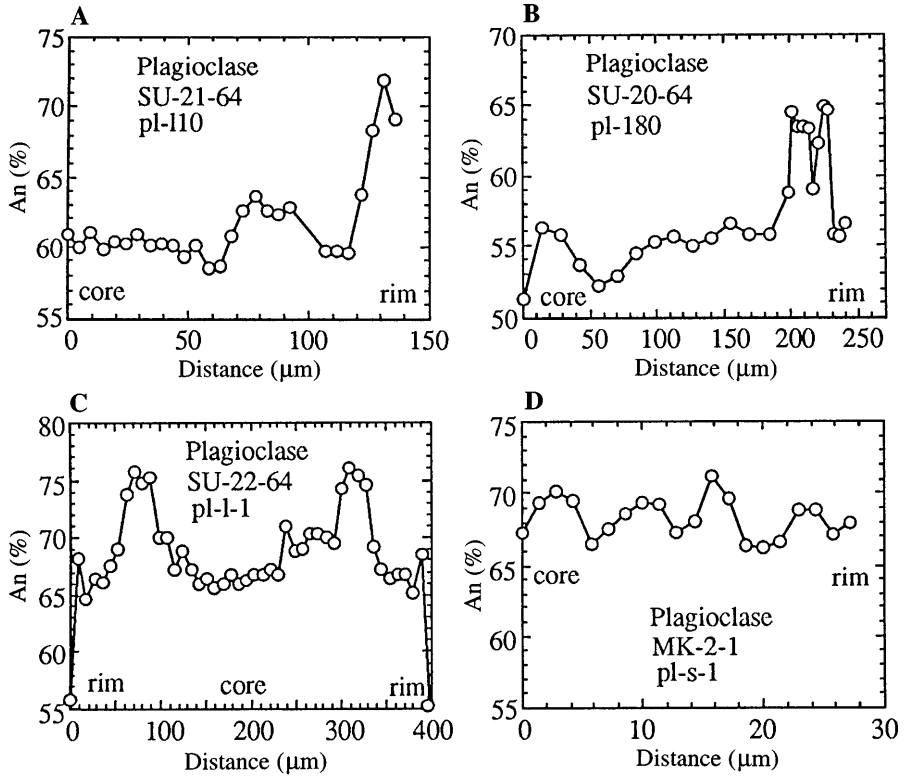

Fig. 7A–D Representative compositional zonation patterns in plagioclase: **A, B** and **C** show large compositional contrast between cores and rims (type I); **D** shows the type II variation which is relatively homogeneous with An% fluctuating within a small range

1992; Helz and Wright 1992). Derivation of these submarine Hilo Ridge lavas from isolated magma chambers is consistent with their significant differences in whole-rock trace element and isotopic characteristics (Yang et al. 1994).

The compositions of the evolved magmas

Because the studied samples represent mixtures of mafic and evolved magmas, the zonation patterns (normal or reverse zoning) of the phenocrysts provide compositional information for the mixing components. Two observations lead us to infer that the differentiated magmas were not in equilibrium with olivine; i.e., they had evolved beyond the reaction point of olivine + melt $\Longrightarrow$low-Ca pyroxene + augite + plagioclase. For example, reversely zoned olivines are absent and unlike the phenocryst cores of augite (Fig. 6) and plagioclase (Fig. 8), the compositions of olivine phenocryst cores do not reflect equilibrium with melts more evolved than the glassy rinds (Fig. 3). The relatively homogeneous pyroxene and plagioclase in MK2-1 (Figs. 6 and 8) indicate that the mixed melt composition, represented by the glassy rind, was buffered near this reaction point. This inference is supported by the relatively high Mg# of orthopyroxene (~81) in this sample (Fig. 10). In contrast, the Fe-rich pyroxene cores and Na-rich plagioclase cores in samples SU-20-64, SU-21-64 and MK1-8 (Figs. 6 and 8) imply that the differentiated magmas had evolved far beyond this reaction point before replenishment. What are the compositions of these evolved magmas? As the glassy pillow rims (mixed melts) contain 5.31 to 6.31% MgO (Yang et al. 1994), the evolved components must have MgO less than this range. However, no evolved glasses or lavas with <5% MgO have been recovered from the Hilo Ridge. Therefore, the core compositions of plagioclase and pyroxenes, which are too enriched in Na and Fe, respectively, to be in equilibrium with the associated glasses (Figs. 6, 8, 10) provide the only clues for the compositions of evolved components.

The MgO contents of melts coexisting with augite can be inferred from the Fe-Mg exchange coefficient (K_D). The lowest Mg# of augite in SU-21-64 and MK1-8 is ~71, corresponding to Mg# of 36–40 in melts (Fig. 11), using a K_D of 0.25 ± 0.2 (Grove et al. 1992; Tormey et al. 1987). An augite in SU-20-64 has Mg# of 63–65 which is in equilibrium with melt having a Mg# of 29–33. Possibly because of their relatively high densities (Brooks et al. 1991), lavas with such iron-rich compositions are rarely erupted during the shield-building stage of Hawaiian volcanoes. A sample from the southwest rift of Kilauea contains 3.9% MgO with a Mg# of 40 (Wright and Fiske 1971), and the uppermost flow on west Molokai has only 4% MgO (D.A. Clague unpublished data). Although not erupted, a lava with 2.26% MgO (Mg# = 33) and 59% SiO_2 is required for the mixing calculation to model Kilauea Yellow Cone lavas (Wright and Fiske 1971). Highly evolved tholeiitic

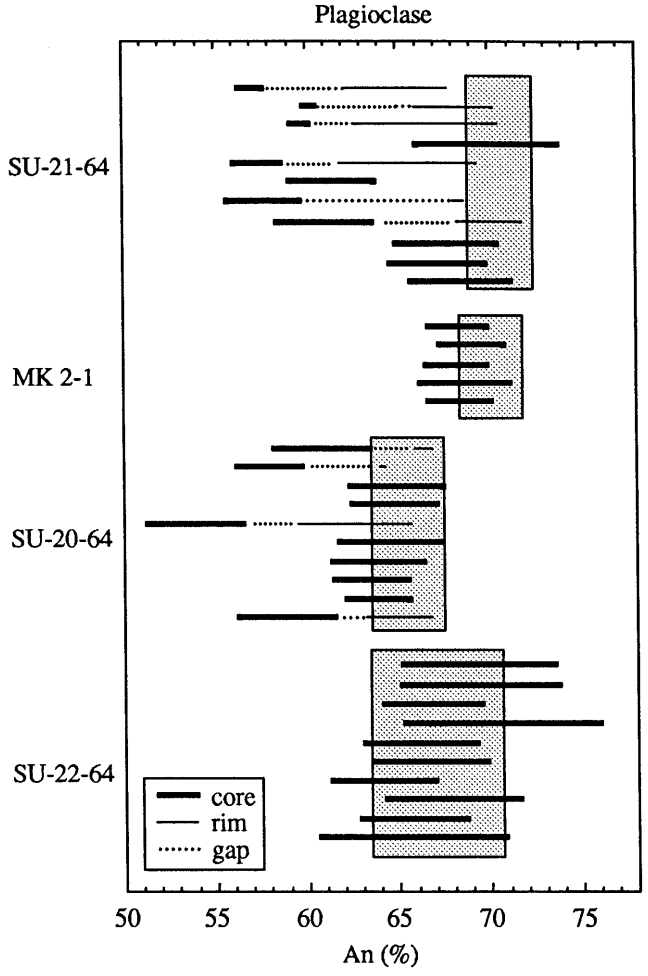

Fig. 8 Plagioclase compositions for four dredged Hilo Ridge samples. Symbols as in Fig. 6. The *box* for each sample is the compositional range in equilibrium with the associated glass calculated from the model of Grove et al. (1992) for 0.001–5 kbar. The range for SU-22-64 is based on the two glass compositions reported by Yang et al. (1994), while those for other samples are calculated for one glass composition

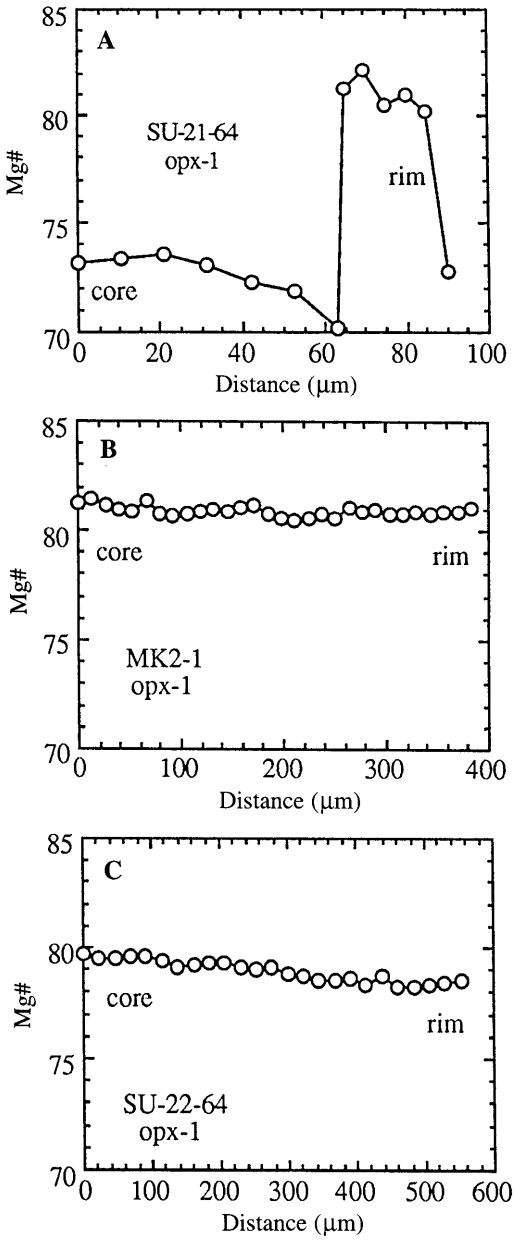

Fig. 9A–C Representative compositional zonation patterns of orthopyroxene: **A** shows the type I variation with a large compositional contrast between rim and core; **B** and **C** show variations in relatively homogeneous grains from samples MK2-1 and SU-22-64

lavas with SiO_2 ranging from 66.1 to 72.5% and MgO ranging from 1.66 to 0.11% were also found at the Kuwale and Kauaopuu Ridges of Waianae volcano on Oahu Island, Hawaii (Bauer et al. 1973; Fodor et al. 1977), and a glass grain from the submarine Puna Ridge of Kilauea contains only 0.98% MgO (D.A. Clague unpublished data). The compositions of augite crystals in Hilo Ridge submarine lavas indicate that such highly evolved melts were also present in this rift zone. On the other hand, the highest Mg# in orthopyroxene, 81–83, which occurs in MK2-1, MK1-8, SU-21-64 and SU-22-64, represents the composition of orthopyroxene that first crystallized from the melt. This can be used to infer the melt composition that was buffered near the reaction point of olivine + melt $\Longrightarrow$low-Ca pyroxene + augite + plagioclase. In these samples, orthopyroxene compositions with Mg# of 81–83 are in equilibrium with their glass rinds (Fig. 10) which contain 5.31 to 6.31% MgO (Mg# = 52).

Equilibrium pressure and temperature

In addition to mineral compositions, mineral-melt equilibration pressure (P) and temperature (T) also bear important information on magma evolution. We determined the equilibrium P-T for the studied samples using the thermobarometers based on clinopyroxene-melt equilibria (Putirka et al. 1996) and empirical equations that relate P-T to the compositions of multiply saturated melts (Kinzler and Grove 1992; Yang et al. 1996). The calculated equilibrium P-T together with petrographic textures provide insight into the crystallization histories of these lavas.

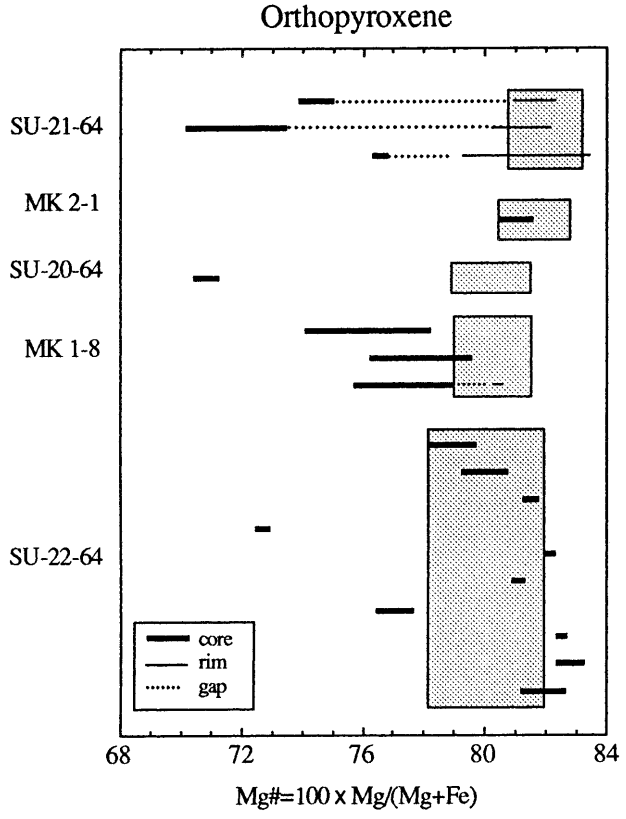

Fig. 10 Orthopyroxene compositions for five dredged Hilo Ridge samples. Symbols as in Fig. 6. The *box* for each sample is the compositional range in equilibrium with the associated glass calculated using $K_D = 0.25 \pm 0.2$ (Grove and Juster 1989). Ferrous iron in melt is assumed to be 85% of total iron

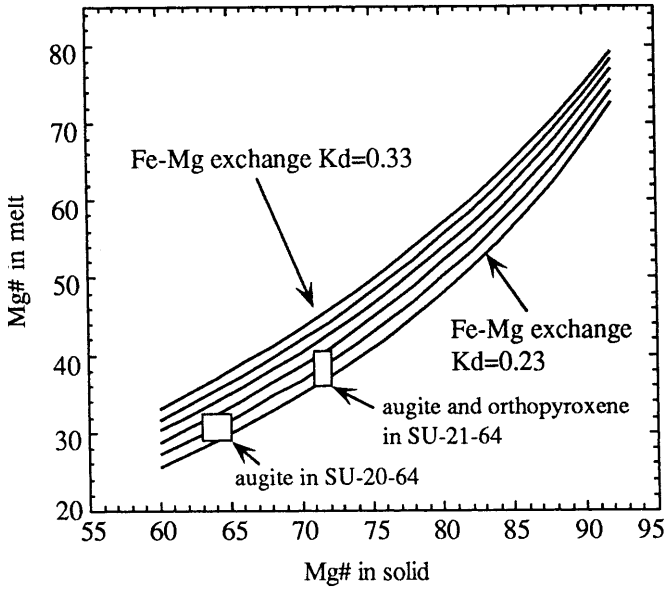

Fig. 11 *Curves* indicate Mg# in coexisting melt and solid. Each curve is calculated with a different Fe-Mg exchange K_D. The *two boxes* are compositions of the most iron-rich augites in SU-20-64 and SU-21-64. The Mg# in their coexisting melts is estimated from $K_D = 0.25 \pm 0.2$

Calculated from clinopyroxene-melt equilibria

Five studied samples contain augite with compositions in equilibrium with residual melts represented by glass rinds (Fig. 6). The *P* and *T* of augite-melt equilibration can be calculated from the thermobarometers of Putirka et al. (1996), which were calibrated with experimentally produced melt compositions and the proportion of jadeite component in the coexisting clinopyroxene. For the Hilo ridge samples the equilibrium composition of each augite grain was derived by averaging all analyses that are in Fe-Mg exchange equilibrium with glass rinds. For the relatively homogeneous augite phenocrysts in MK2-1 and SU-22-64 (Fig. 6), all analyses in a grain were averaged. In samples MK1-8, SU-21-64 and SU-20-64, only the rim compositions were selected. Also in samples SU-20-64 and SU-21-64 augite rims on orthopyroxene were used. In sample SU-22-64, the augite rims enclosing orthopyroxene crystals show systematic increases of jadeite component from the inner clinopyroxene/orthopyroxene contacts towards the outer edges of augite rims. We infer that only the outermost rims were in equilibrium with the glassy rinds and their compositions were also used for calculations.

Using the preferred equations (P1 and T2) of Putirka et al. (1996), we find that most of the analyzed augite crystals were last equilibrated at 2–3 kbar and 1130–1150 °C. Some estimates extend to 3–4 kbar and 1155–1165 °C. Only two augite crystals have low equilibrium pressures of ~1 kbar. The equilibrium *P-T* of the augite rims on orthopyroxene crystals are similar to those of individual augite crystals except for sample SU-22-64 where several augite rims yield pressure estimates of 4.1 to 4.9 kbar (Table 5).

The *P* estimates for MK1-8 in Table 5 contrast with the 7.5 kbar estimate for MK1-8 reported in Table 1 of Putirka (1997). This 7.5 kbar estimate was based on clinopyroxene core compositions and the whole-rock composition reported in Frey et al. (1991). We note that these cores are not in Fe/Mg equilibrium with a melt having the whole-rock composition. Moreover, the whole-rock composition reflects magma mixing (Yang et al. 1994); therefore, the whole-rock composition is not suitable for such calculations (Putirka 1997). Consequently, we suggest that the lower *P* estimate of 2.7 kbar in Table 5 is more realistic.

Calculated from multiple-saturated melt compositions

The estimates based on the thermobarometer of Putirka et al. (1996) were compared with results obtained from the empirical expressions of Kinzler and Grove (1992; abbreviated as KG92), which relate equilibrium *P-T* of phenocryst formation to compositions of multiply saturated melts. The KG92 equations describe *T* as well as the olivine, plagioclase, clinopyroxene and quartz components of an olivine-plagioclase-augite-low-Ca pyrox-

Table 5 Equilibrium pressures and temperatures of Hilo Ridge submarine lavas (see text for detailed descriptions of methods)

	P (kbar)	*T* (°C)
MK2-1		
Calculated with cpx-melt equilibria[a]		
Cpx-1 bulk composition	2.2	1146
Cpx-2 bulk composition	2.3	1148
Cpx-3 bulk composition	2.9	1151
Cpx-5 bulk composition	2.8	1149
Cpx-6 bulk composition	2.6	1148
Average	2.6	1148
Calculated with KG92 model[b]		
	3.2	1171
MK1-8		
Cpx-1 rim composition	1.7	1127
Cpx-3 rim composition	2.6	1133
Cpx-5 rim composition	2.1	1130
Cpx-131 rim composition	3.4	1139
Cpx-129 rim composition	1.6	1125
Cpx-132 rim composition	2.5	1132
Cpx-133 rim composition	3.8	1144
Cpx-136 rim composition	3.7	1143
Average	2.7	1134
Calculated with KG92 model		
	1.4	1144
SU-21-64		
Cpx-1 bulk composition	2.2	1148
Cpx-2 bulk composition	3.1	1157
Cpx-3 bulk composition	3.6	1160
Cpx-5 bulk composition	3.0	1155
Cpx-6 bulk composition	3.8	1161
Cpx-7 bulk composition	4.1	1163
Cpx-9 bulk composition	2.1	1147
Average	3.1	1156
Cpx-11 rim on opx	3.0	1159
Cpx-10 rim on opx	3.5	1163
Calculated with KG92 model		
	1.0	1153
SU-20-64		
Calculated with cpx-melt equilibria		
Cpx-1 rim composition	2.5	1136
Cpx-2 rim composition	2.8	1139
Cpx-5 rim composition	2.3	1135
Cpx-15 rim composition	1.1	1128
Cpx-16 rim composition	1.8	1133
Average	2.1	1134
Cpx-3 rim on opx	3.0	1142
Cpx-6 rim on opx	2.0	1132
Calculated with KG92 model		
	1.6	1147
Calculated with YKG96 model[c]		
	0.001	
SU-22-64		
Calculated with cpx-melt equilibria		
Cpx-1 bulk composition	2.2	1128
Cpx-2 bulk composition	3.2	1138
Cpx-3 bulk composition	3.6	1139
Cpx-5 bulk composition	3.3	1135
Cpx-6 bulk composition	1.1	1120
Cpx-7 bulk composition	1.9	1126
Average	2.6	1131
Cpx rim on opx-1	4.8	1149
Cpx rim on opx-2	4.1	1142
Cpx rim on opx-3	4.9	1149
Cpx rim on opx-5	4.9	1150
Cpx rim on opx-7	1.1	1118
Cpx rim on opx-8	3.7	1138
Cpx rim on opx-9	4.8	1150
Cpx rim on opx-11	2.5	1130
Calculated with KG92 model		
	6.5	1190
	5.0	1172
Calculated with YKG96 model		
	2.0	

[a] Equilibrium *P* and *T* are calculated with the thermobarometer of Putirka et al. (1996)
[b] Equilibrium *P* and *T* are calculated with the equations of Kinzler and Grove (1992)
[c] Equilibrium *P* and *T* are calculated with the model of Yang et al. (1996)

ene-saturated melt as a function of *P*, Mg#, NaK# $[(Na_2O + K_2O)/(Na_2O + K_2O + CaO)]$ and TiO_2% of the melt. These equations were developed to model partial melting of spinel and plagioclase lherzolite rather than partial crystallization of basaltic magmas. Our objective is to use these equations with the glassy rim compositions of Hilo Ridge lavas to calculate the *P-T* for four-phase saturation. In order to evaluate the suitability of the KG92 equations for crystallization of a basaltic system, we compare the calculated *P-T* to the equilibrium *P-T* of ML-16 which is a multiply saturated melt experimentally produced from a Mauna Loa lava (ML-206) at 1 atmosphere and 1140 °C (Montierth et al. 1995). Olivine was not present at 1140 °C, but no four-phase saturated melt was produced in the liquid line of descent study of Montierth et al. (1995). Sample ML-16 is the highest temperature melt that contains plagioclase, augite and low-Ca pyroxene during the crystallization of sample ML-206. It is reasonable to infer that this melt is close to the multiple saturation surface of olivine, plagioclase, augite and low-Ca pyroxene. With the glass composition of ML-16 at 1140 °C, the pressures obtained from the quartz, plagioclase, olivine and clinopyroxene KG92 equations are 1.3, 0.4, 0.3 and 1.7 kbar, respectively. The calculated four-phase saturation temperature for ML-16 is 1135 °C at 0.001 kbar and 1144 °C at 1 kbar. In general, the predicted values agree with the experimental results thereby indicating that KG92 equations are appropriate for multiply saturated Hawaiian lavas. Applying the KG92 equations to the Hilo Ridge samples, we find that pressures calculated from the plagioclase equation usually agree with values from olivine or quartz equations, a result similar to that for ML-16. The discrepancy between the value obtained from the clinopyroxene equation and those from the other three equations can be as large as 4 kbar. The clinopyroxene equation was also the most disparate for ML-16. Therefore, the pressure estimates from the clinopyroxene equation are not considered in the following discussion.

Based on KG92 equations, samples MK1-8, MK2-1, SU-21-64 and SU-20-64 were multiply saturated with olivine, plagioclase, clinopyroxene and low-Ca pyroxene at 1–3 kbar and 1144–1171 °C while sample SU-22-64 coexisted with these four phases at relatively higher *P-T* of 5–6.5 kbar and 1172–1190 °C (Table 5). It is important to integrate *P-T* estimates with petrographic observations. For all studied samples, the petrography indicates that olivine, plagioclase and augite were stable in the residual melts, i.e., the glassy rinds. In contrast, the textural characteristics of orthopyroxene are more complex. For samples MK1-8, MK2-1 and SU-21-64, the orthopyroxene rims were in equilibrium with residual melts (Fig. 10). Therefore, for these three samples, the *P-T* estimates derived from augite-melt equilibria (Putirka et al. 1996) and the KG92 equations should agree. Although there is a good agreement for *T*, the KG92 equations yield lower *P* estimates for MK1-8 (1.4 vs 2.7 kbar) and SU-21-64 (1.0 vs 3.1 kbar) and slightly higher *P* for MK2-1 (3.2 vs 2.6 kbar). Despite the differences of up to 2 kbar, it is evident that the glasses and phenocryst rims in these samples reflect relatively low equilibrium *P* of ≤3 kbar.

The orthopyroxene crystals in samples SU-20-64 and SU-22-64, however, were not in equilibrium with the glassy rinds because these orthopyroxenes reacted with melt to form augite rims (Fig. 4 E–H). For these two samples, the KG92 model predicts the *P-T* at which their glass compositions would coexist with olivine-plagioclase-augite-orthopyroxene. Since the glasses in samples SU-20-64 and SU-22-64 were only saturated with olivine, plagioclase and augite, the Yang et al. (1996; abbreviated as YKG96) model is more appropriate for calculating equilibrium *P-T*. Based on this model, the equilibrium *P* is 0.001 kbar for SU-20-64 and 2 kbar for SU-22-64. These *P* estimates from the YKG96 model are consistent with estimates from Putirka's thermobarometer within an uncertainty of ±1 kbar (Table 5).

In summary, the equilibrium *P-T* calculated from different thermobarometers can be integrated to constrain the crustal evolution of these rift zone lavas. The phenocryst assemblages reflect equilibration at < 3 kbar and similarly low pressures are indicated by the clinopyroxene and glass compositions in samples SU-20-64, MK2-1 and MK1-8. However, several clinopyroxenes in samples SU-21-64 and SU-22-64 have compositions that reflect equilibration at higher pressures, up to 4.9 kbar for SU-22-64 (Table 5).

Magma migration pathways: inferences from the equilibration pressure of sample SU-22-64

It is probably not coincidental that sample SU-22-64 which reflects the highest equilibration pressure also has a distinctive whole-rock composition. Among these dredged lavas, it has the lowest Zr/Nb ratio and highest La/Yb ratio; these are geochemical characteristics consistent with a relatively low extent of melting

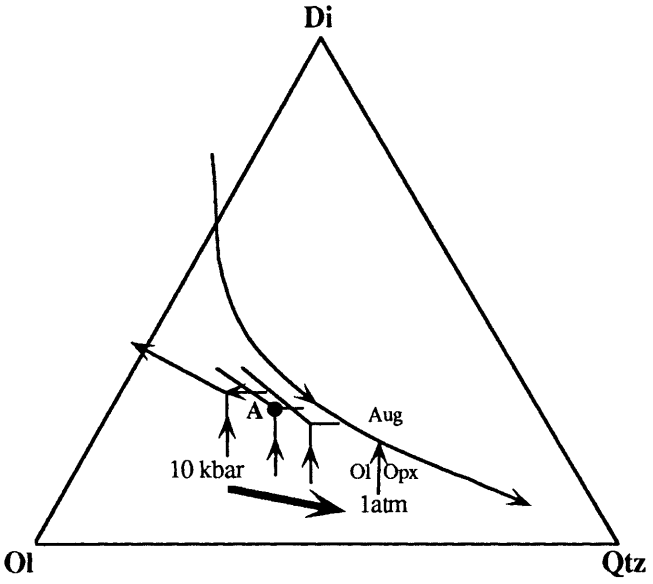

Fig. 12 An illustrative olivine (*Ol*)-diopside (*Di*)-quartz (*Qtz*) pseudoternary [projected from the plagioclase (*Plag*) corner of the Ol-Di-Qtz-Plag tetrahedron onto the Ol-Di-Qtz plane] modified from Stolper (1980). The 10 kbar and 1 atmosphere cotectic boundaries of Stolper (1980) were used to infer the cotectic boundaries between these two pressures. As pressure decreases, the multiple-saturation point shifts towards the Qtz corner as indicated by the *thick arrow*. *Point A* represents a melt saturated with olivine, augite and orthopyroxene at a relatively high pressure. As pressure decreases, melt with the composition of point A changes from 4-phase saturated (olivine-plagioclase-augite-orthopyroxene) to 3-phase saturated then to saturation with only plagioclase and olivine

(Yang et al. 1994). This sample also has a relatively low SiO_2 content which may reflect melt segregation or crystal fractionation at high pressures (Langmuir et al. 1992; Yang et al. 1994). Sample SU-22-64 contains the most abundant orthopyroxene; abundant orthopyroxene in a low SiO_2 magma is consistent with high pressure crystal fractionation. Based on experimental studies (e.g., Stolper 1980), the olivine primary field shrinks at high pressure and the four-phase multiple saturation point moves away from silica (Fig. 12), thereby, decreasing the SiO_2 content of the multiply saturated melts. During ascent to lower pressures, a low SiO_2 melt saturated with olivine, augite and orthopyroxene (point A in Fig. 12) becomes undersaturated with respect to orthopyroxene and perhaps augite (e.g., in Fig. 12 point A lies close to the olivine-augite cotectic at a lower pressure). With further ascent to lower pressures, the composition of this melt is within the primary field of olivine and only olivine crystallizes (in Fig. 12 at 1 atmosphere, point A is in the olivine primary field). This crystallization sequence can explain the pyroxene-olivine relationships found in this sample (Fig. 4H). Although magma mixing is consistent with the reverse zoning in plagioclase (Fig. 7C) and may explain orthopyroxene rimmed by fine-grained augites and olivines, mixing at low pressures cannot readily explain orthopyroxene rimmed with only fine-grained olivines in the outermost edge (Fig. 4H). Such a texture

cannot result from magma mixing, because a hybrid magma with low MgO content (5.60–5.44%; Table 3b of Yang et al. 1994) is unlikely to crystallize only olivine. Note that most of the pyroxenes in SU-22-64 have Mg# varying over a small range, similar to that of MK2-1 (Figs. 6 and 10). Like MK2-1, this sample may have been buffered at the olivine + melt $\Longrightarrow$low-Ca pyroxene + augite + plagioclase reaction point but at a higher pressure. Subsequently, the complex textures associated with orthopyroxene developed while this magma ascended to lower pressures.

Calculated equilibrium pressures of ~5 kbar for sample SU-22-64 provide evidence for high pressure crystallization (Fig. 1). A possible pathway is that some magmas bypass the shallow summit reservoir and migrate laterally into the rift zones along the oceanic crust-mantle boundary (Fig. 1). Geophysical studies show that below rift zones the transition from Hawaiian lavas to pre-existing oceanic crust is at ~9 to 11 km below sea level and that the oceanic crust-mantle boundary is at 15 to 20 km (Delaney et al. 1990; Moore 1987; Okubo et al. 1997; Tilling and Dvorak 1993). Therefore equilibration pressures of ~5 kbar for a rift zone magma may reflect magma migration along the oceanic crust-mantle boundary. Garcia et al. (1995) proposed a similar model for the Southwest Rift of Mauna Loa. Putirka (1997) argued that clinopyroxenes in magmas ascending to a shallow summit reservoir prior to lateral migration into a rift zone can retain a high pressure signature. We think that this pathway is unlikely for sample SU-22-64 because the high pressure signature is present only in clinopyroxene rims on orthopyroxene; such rims are unlikely to survive during a protracted low pressure magma migration path (Fig. 1). In addition, the distinctive geochemical characteristics of SU-22-64 (i.e., low SiO_2 and Zr/Nb and high La/Yb) which we attribute to high pressure processes are consistent with a distinct magma ascent pathway.

Putirka (1997) used data for the Pu'u O'o east rift eruption of Kilauea to argue that high *P* clinopyroxene can survive during ascent of magma to the shallow Kilauea summit reservoir and subsequent transport to and eruption on the rift zone. Specifically, a systematic increase in calculated equilibration pressure of pyroxene ranging from 0.4 kbar when the eruption began to 20 kbar 270 days later was interpreted as tapping of increasingly deeper magmas stored beneath the summit reservoir. These lavas were erupted during episodes when there were large compositional variations (7–10 wt% MgO) and the mineralogy shifted over a few hours to clinopyroxene-free, more mafic composition as the local shallow reservoir was tapped (< 3 km; Hoffman et al. 1990; Garcia et al. 1992). The compositional zoning in these mostly microphenocrysts was interpreted to have formed under rapid quenching (Garcia et al. 1992); consequently, they may not be suitable for geothermobarometry calculations. It is apparent that rigorous constraints on magma ascent paths for Hawaiian rift zone magmas retaining a relatively high *P* signature require additional studies of phenocryst compositions and simultaneous applications of several geothermobarometers.

Comparison with lavas recovered from submarine rift zones of Kilauea and Mauna Loa

Like the Hilo Ridge submarine samples, lavas dredged from Kilauea's Puna Ridge and Mauna Loa's Southwest rift zone contain olivine, plagioclase and augite phenocrysts (Clague et al. 1995; Garcia et al. 1995). Orthopyroxene also occurs in some of these lavas. Pigeonite is rare and was found in only two Puna Ridge samples (Clague et al. 1995). The compositional ranges and zoning patterns of phenocrysts in lavas from these rift zones reflect both similarities and differences in the evolution of magmas along these rift zones.

In contrast to normally zoned olivine phenocrysts in Hilo Ridge lavas, about 20% of the olivine phenocrysts analyzed from Kilauea's Puna Ridge show reverse zoning (Clague et al. 1995) indicating magma chamber replenishment by mafic magmas before evolution of the chamber magmas beyond the olivine + melt $\Longrightarrow$ low-Ca pyroxene reaction point. However, augite, plagioclase and orthopyroxene phenocrysts in Puna Ridge lavas have compositional ranges and zoning patterns similar to those in Hilo Ridge lavas. Clague et al. (1995) reported that some Puna Ridge lavas contain reversely zoned augite and orthopyroxene with a large range of Mg#, 63–84, while other samples have relatively homogeneous pyroxene with Mg# varying from 78 to 84. To evaluate further the similarity with Hilo Ridge samples, we studied a Puna Ridge sample. Augite phenocrysts in this sample show an abrupt increase in Mg# from cores (Mg# = 63–72) to rims (Mg# = ~84) (Figs. 5 and 6). The Fe-rich cores are comparable to the most Fe-rich augite core in Hilo Ridge sample, SU-20-64 (Fig. 6) and the zonation mimics that of the type I augite in Hilo Ridge lavas (Fig. 5). Also similar to Hilo Ridge sample SU-20-64, the plagioclase phenocrysts in Puna Ridge lavas associated with Fe-rich pyroxene cores are enriched in albite ($An_{47–55}$) (Clague et al. 1995). These similarities show that similar magmatic processes operated in both of these submarine rifts; in particular, highly evolved melt compositions formed in both rifts. Although not commonly erupted as homogeneous magmas, these highly evolved melts are manifested as mixing endmembers in the erupted lavas.

The submarine lavas from the Southwest Rift of Mauna Loa contain olivine crystals varying from Fo_{77} to Fo_{91}, similar to those in Hilo and Puna Ridge lavas. All of the analyzed olivine from Mauna Loa's Southwest Rift are normally zoned, except for a few low Fo grains ($<Fo_{84}$) which are slightly reversely zoned with Fo content varying within 2% (Garcia et al. 1995). Although the dominance of normally zoned olivine is similar to Hilo Ridge lavas, the relatively homogeneous

pyroxenes (Mg# = 76–83), and plagioclase ($An_{67–78}$) in these lavas (Garcia et al. 1995) contrast with the large compositional variations of these minerals in Hilo and Puna Ridge lavas. Some lavas from the Southwest Rift have reversely zoned pyroxene, but there is no evidence for the highly evolved magmas which were mixing end-members in the Hilo and Puna Ridge lavas. A plausible interpretation is that the magma supply rate at the Southwest Rift zone is sufficient to keep magma chambers from evolving beyond the olivine + melt low-Ca pyroxene reaction point.

Using the equations of Kinzler and Grove (1992), we find that the four-phase saturated lavas from the Puna Ridge and Southwest Rift reflect phenocryst equilibration at ~2 kbar. No high pressure melt, such as Hilo Ridge sample SU-22-64, has been sampled at these other rift zones. Therefore, the phenocryst assemblages and compositions in most rift zone magmas reflect equilibration at ~2 kbar (6 km).

Concluding remarks

The submarine-erupted lavas recovered from the Hilo Ridge rift zone are MgO-rich (11–20%) tholeiites whose phenocryst compositions document a complex petrogenesis involving magma mixing (Yang et al. 1994). The reversely zoned compositions of plagioclase and pyroxene phenocrysts indicate the presence of evolved magmas which were not erupted. For example, the cores of clinopyroxene phenocrysts in two of these lavas equilibrated with melts having Mg# of 29 to 33. During the shield building stage of Hawaiian volcanoes eruption of such low (<5%) MgO lavas is uncommon (e.g., Wright and Fiske 1971), but such lavas may develop during periods of low magma supply in the distal parts of rift zones. The differences in the mineral compositions and zoning profiles between samples provide evidence that these samples were derived from isolated magma chambers which had undergone distinct fractionation and mixing histories. Each magma chamber was recharged several times before eruption. Based on the compositions of augite rims and the associated glass rinds, the five studied samples were last equilibrated at pressures < 3 kbar. Sample SU-22-64 shows evidence of crystallization at higher pressures (4–5 kbar). Equilibration pressures of < 3 kbar are consistent with intrusions of summit reservoir magmas (2–7 km) into rift zones. However, the ~15 km depth of the oceanic crust- mantle boundary beneath rift zones and magma equilibration pressures of 4 to 5 kbar indicate that some magmas may be transported into the rift zone along the crust-mantle boundary (Fig. 1, this paper and Fig. 12 of Garcia et al. 1995).

Acknowledgments We thank Neel Chatterjee and Glenn Gaetani for their help in electron microprobe analysis, Timothy Grove for his comments on an early version of manuscript and Keith Putirka for providing the spreadsheet for the clinopyroxene-melt thermobarometer. We thank an anonymous reviewer, and especially Keith Putirka for a comprehensive and constructive review. This research is supported by NSF Grant EAR-875809 to F.A. Frey and EAR-9614247 to M.O. Garcia. This is SOEST Contribution 4761.

References

Albee AL, Ray L (1970) Correction factors for electron microprobe analysis of silicates, oxides, carbonates, phosphates and sulfates. Anal Chem 42: 1408–1414

Bauer GR, Fodor RV, Hustler JW, Keil K (1973) Contributions to the mineral chemistry of Hawaiian rocks. III. Composition and mineralogy of a new rhyodacite occurrence on Oahu, Hawaii. Contrib Mineral Petrol 40: 183–194

Bence AE, Albee AL (1968) Empirical correction factors for the electron microanalysis of silicates and oxides. J Geol 76: 382–403

Brooks CK, Larsen LM, Nielsen TFD (1991) Importance of iron-rich tholeiitic magmas at divergent plate margins: a reappraisal. Geology 19: 269–272

Clague DA, Moore JG, Dixon JE, Friesen WB (1995) Petrology of submarine lavas from Kilauea's Puna Ridge, Hawaii. J Petrol 36: 299–349

Delaney PT, Fiske RS, Miklius A, Okamura AT, Sako MI (1990) Deep magma body beneath the summit and rift zones of Kilauea volcano, Hawaii. Science 247: 1311–1316

Dungan MA, Rhodes JM (1978) Residual glasses and melt inclusion in basalts from DSDP Legs 45 and 46: evidence for magma mixing. Contrib Mineral Petrol 67: 417–431

Dvorak JJ, Dzurisin D (1993) Variations in magma supply rate at Kilauea volcano, Hawaii. J Geophys Res 98: 22255–22268

Fodor RV, Keil K, Bauer GR (1977) Contributions to the mineral chemistry of Hawaiian rocks. V. Compositions and origin of ultramafic nodules and megacrysts in a rhyodacite from Oahu, Hawaiian Islands. Pac Sci 31: 211–222

Frey FA, Garcia MO, Wise WS, Kennedy A, Gurriet P, Albarède F (1991) The evolution of Mauna Kea volcano, Hawaii: petrogenesis of tholeiitic and alkalic basalts. J Geophys Res 96: 14347–14375

Garcia MO (1996) Petrography, olivine and glass chemistry of lavas from the Hawaii Scientific Drilling Project. J Geophys Res 101: 11701–11713

Garcia MO, Muenow D, Aggrey KE, O'Neil J (1989) Major element, volatile, and stable isotope geochemistry of Hawaiian submarine tholeiitic glasses. J Geophys Res 94: 10525–10538

Garcia MO, Rhodes JM, Wolfe EW, Ulrich GE, Ho RA (1992) Petrology of lavas from episodes 2–47 of the Puu Oo eruption of Kilauea volcano, Hawaii: evaluation of magmatic processes. Bull Volcanol 55: 1–16

Garcia MO, Hulsebosch TP, Rhodes JM (1995) Olivine-rich submarine basalts from the southwest rift zone of Mauna Loa volcano: implications for magmatic processes and geochemical evolution. Am Geophys Union Geophys Monogr 92: 219–239

Grove TL, Juster TC (1989) Experimental investigations of low-Ca pyroxene stability and olivine-pyroxene-liquid equilibria at 1 atm in natural basaltic and andesitic liquids. Contrib Mineral Petrol 103: 287–305

Grove TL, Kinzler RJ, Bryan WB (1992) Fractionation in mid-ocean ridge basalts (MORB). Am Geophys Union Geophys Monogr 71: 281–310

Helz RT, Thornber CR (1987) Geothermometry of Kilauea Iki lava lake, Hawaii. Bull Volcanol 49: 651–668

Helz RT, Wright TL (1992) Differentiation and magma mixing on Kilauea's east rift zone: a further look at the eruptions of 1955 and 1960. I. The late 1955 lavas. Bull Volcanol 54: 361–384

Hoffman J, Ulrich G, Garcia MO (1990) Horizontal ground deformation patterns and magma storage during the Pu'u O'o eruption, Kilauea volcano, Hawaii: episodes 22–42. Bull Volcanol 52: 522–531

Juster TC, Grove TL (1989) Experimental constraints in the generation of Fe-Ti basalts, andesites, and rhyodacites at the Galapagos spreading center, 85°W and 95°W. J Geophys Res 94: 9251–9274

Kinzler RJ, Grove TL (1992) Primary magmas of mid-ocean ridge basalts. 1. Experiments and methods. J Geophys Res 97: 6885–6906

Klein FW, Koyanagi RW, Nakata JS, Tanigawa WR (1987) The seismicity of Kilauea's magma system. US Geol Surv Prof Pap 1350: 1019–1185

Kuo L-C, Kirkpatrick RJ (1982) Pre-eruption history of phyric basalts from DSDP Legs 45 and 46: evidence from morphology and zoning pattern in plagioclase. Contrib Mineral Petrol 79: 13–27

Langmuir CH, Klein EM, Plank T (1992) Petrological systematic of mid-ocean ridge basalts: constraints on melt generation beneath ocean ridges. Am Geophys Union Geophys Monogr 71: 183–280

Lassiter JC, DePaolo DJ, Tatsumoto M (1996) Isotopic evolution of Mauna Kea volcano: results from the initial phase of the Hawaii Scientific Drilling Project. J Geophys Res 101: 11769–11780

Montierth C, Johnston AD, Cashman KV (1995) An empirical glass-composition-based geothermometer from Mauna Loa lavas. Am Geophys Union Geophys Monogr 92: 207–217

Moore JG (1966) Rate of palagonitization of submarine basalt adjacent to Hawaii. US Geol Surv Prof Pap 550-D: 163–171

Moore JG (1987) Subsidence of the Hawaiian Ridge. US Geol Surv Prof Pap 1350: 85–100

Moore JG, Clague DA (1992) Volcano growth and evolution of the island of Hawaii. Geol Soc Am Bull 104: 1471–1484

Moore JG, Fiske RS (1969) Volcanic substructure inferred from dredge samples and ocean-bottom photographs, Hawaii. Geol Soc Am Bull 80: 1191–1202

Murata KJ, Richter DH (1966) Chemistry of the lavas of 1959–1960 eruption of Kilauea volcano, Hawaii. US Geol Surv Prof Pap 537-A

Okubo PG, Benz HM, Chouet BA (1997) Imaging the crustal magma sources beneath Mauna Loa and Kilauea volcanoes, Hawaii. Geology 25: 867–870

Putirka K (1997) Magma transport at Hawaii: inferences based on igneous thermobarometer. Geology 25: 69–72

Putirka K, Johnson M, Kinzler R, Longhi J, Walker D (1996) Thermobarometry of mafic igneous rocks based on clinopyroxene-liquid equilibria, 0–30 kbar. Contrib Mineral Petrol 123: 92–108

Reiners PW, Sawyer N-L, Nelson BK, Holcomb RT (1997) Alkalic and tholeiitic submarine lavas from the Hilo Ridge rift zone, Hawaii: implications for the evolution of Mauna Kea volcano. EOS Trans Am Geophys Union 78: F645

Rhodes JM (1988) Geochemistry of the 1984 Mauna Loa eruption: implication for magma storage and supply. J Geophys Res 93: 4453–4466

Rhodes JM, Dungan MA, Blanchard DP, Long PE (1979) Magma mixing at mid-ocean ridges: evidence from basalts drilled near 22°N on the mid-Atlantic ridge. Tectonophysics 55: 35–61

Ryan MP, Koyanagi RY, Fiske RS (1981) Modeling the three-dimensional structure of macroscopic magma transport systems: application to Kilauea volcano. J Geophys Res 86: 7111–7129

Stolper E (1980) A phase diagram for mid-ocean ridge basalts: preliminary results and implications for petrogenesis. Contrib Mineral Petrol 74: 13–27

Tilling RI, Dvorak JS (1993) Anatomy of a basaltic volcano. Nature 363: 125–133

Tormey DR, Grove TL, Bryan WB (1987) Experimental petrology of normal MORB near the Kane Fracture Zone: 22°N–25°N, mid-Atlantic ridge. Contrib Mineral Petrol 96: 121–139

Wright TL, Fiske RS (1971) Origin of differentiated and hybrid lavas of Kilauea volcano, Hawaii. J Petrol 12: 1–65

Yang H-J, Frey FA, Garcia MO, Clague DA (1994) Submarine lavas from Mauna Kea volcano, Hawaii: implications for Hawaiian shield-stage processes. J Geophys Res 99: 15577–15594

Yang H-J, Kinzler RJ, Grove TL (1996) Experiments and models of anhydrous olivine-plagioclase-augite-saturated melts from 0.001–10 kbar. Contrib Mineral Petrol 124: 1–18